Geometric Constraint Based Modeling and Analysis of a Novel Continuum Robot with SMA Initiated Variable Stiffness

Chenghao Yang [1,4], Shineng Geng [1], Ian Walker [2], David T Branson [3], Jinguo Liu [4], Jian S Dai [1,5], Rongjie Kang [1,*]

[1] Key Laboratory of Mechanism Theory and Equipment Design of the Ministry of Education, Centre for Advanced Mechanisms and Robotics, Tianjin University, China
[2] Department of Electrical and Computer Engineering, Clemson University, U.S.A.
[3] Faculty of Engineering, University of Nottingham, U.K.
[4] State Key Laboratory of Robotics, Shenyang Institute of Automation, Chinese Academy of Sciences, China
[5] Centre for Robotics Research, King's College London, U.K.

Abstract
Continuum robots exhibit promising adaptability and dexterity for soft manipulation due to their intrinsic compliance. However, this compliance may lead to challenges in modeling as well as positioning and loading. In this paper, a virtual-work based static model is established to describe the deformation and mechanics of continuum robots with a generic rod-driven structure, taking the geometric constraint of the drive rods into account. Following this, this paper presents a novel variable-stiffness mechanism powered by a set of embedded Shape Memory Alloy (SMA) springs, which can make the drive rods 'locked' on the body structure with different configurations. The resulting effects of variable stiffness are then presented in the static model by introducing tensions of the SMA and friction on the rods. Compared with conventional models, there is no need to predefine the actuation forces of the drive rods, but only actuation displacements are used in this new mechanism system with stiffness being regulated. As a result, the phenomenon that the continuum robot can exhibit an S-shaped curve when subject to single-directional forces is observed and analyzed. Simulations and experiments demonstrated that the presented mechanism has the stiffness variation over 287% and further demonstrated that the mechanism and its model are achievable with good accuracy that the ratio of positioning error has less than 2.23% at the robot end-effector to the robot length.

Keywords:
Soft continuum robot; Variable stiffness; Statics model; Geometric constraint;

1. Introduction

Inspired by biological tentacles or snakes, soft continuum robots possess theoretically infinite degrees of freedom (DOF), intrinsic compliance, and splendid adaptability, which extends the capabilities of traditional rigid robots, in areas such as detection in unstructured environments and grasping non-cooperative targets with few sensors equipped (Rone and Ben-Tzvi, 2014b; Simaan et al., 2009; Deimel and Brock, 2016). Since the concept, first proposed by Robinson et al. (1999), various types of continuum robots have emerged in the past years but can be categorized roughly in terms of their actuation mechanisms as cable-driven (rod-driven) type (McMahan et al.,

* Corresponding author.

2005; Dong et al., 2017; Kato et al., 2015; Rone and Ben-Tzvi, 2014b; Simaan et al., 2009; Zhang et al., 2016; Catalano et al., 2014), pneumatically-driven type (Walker et al., 2005; Kim et al., 2014a; Kang et al., 2013; Hawkes et al., 2017) and concentric-tube type (Dupont et al., 2010; Webster et al., 2009; Rucker et al., 2010). However, their flexible structures make it difficult for all types of soft continuum robots to withstand large forces and keep motion precision at the same time (Dai and Ding, 2005). These defects have driven researchers to focus on the design of variable stiffness mechanisms (Cianchetti et al., 2014). In recent years, several stiffness control methods for continuum manipulators have been studied, and can be classified into two categories: algorithm-based and mechanism-based methods.

Using active control algorithms at actuation level to change the stiffness characteristics of continuum manipulators originates from the impedance control or hybrid motion/force control in traditional rigid robots but the strain energy was also taken into account (Mahvash and Dupont, 2011; Bajo and Simaan, 2016). These methods were usually performed by detecting/estimating the position and contact force at arm tip and calculate the corresponding control variables in a closed-loop way, which is complex and time-consuming for the controller.

Mechanism-based methods have also been used in numerous prior works, as summarized in Table 1. The idea of antagonistic actuators is to increase the internal stress of the structure by applying a pair of opposing forces. Stilli et al. (2014) implemented pneumatic and tendon-driven actuators to control the stiffness of soft manipulators. Kim et al. (2014b) proposed a continuum manipulator for minimally invasive surgery, which can adjust its stiffness by tensioning all the cables along the robot simultaneously, but high tension may cause structural buckling. A slide-linkage locking mechanism was proposed by Yagi et al. (2006) for a flexible endoscopic manipulator that increases rigidity by meshing the racks embedded in adjacent segments. Sun et al. (2020) proposed a hybrid continuum robot based on pneumatic muscles with embedded elastic rods, which can enhance stiffness by locking the rods to the robot base. Note that, these mechanisms are relatively large in size or heavy in weight. A central-cable-tensioning mechanism was designed by Degani et al. (2006) for a continuum endoscope whose stiffness can intensify under the tension of a built-in cable passing through the central axis of the robot. A similar design was used in a tension-stiffening continuum catheter made of a series of spherical joints connected end to end (Chen et al., 2010). These mechanisms are feasible to implement but it remains difficult to evenly distribute the tension of the built-in cable along the arm, which means that the stiffness change on the joints might be unequal, especially when the arm bends. Moreover, such mechanisms will occupy the central channel of the continuum manipulators and make it difficult to route tubing to the end effector. Jamming based mechanisms can stiffen the robots without affecting their position and shape. Cheng et al. (2012) and Ranzani et al. (2015) combined soft continuum robots with a granular jamming-based stiffening mechanism. In addition, several tension cables were further used to strengthen the jammed body (Cheng et al., 2012). However, the above approaches may make the robots less compact. Kim et al. (2013), Moses et al. (2013) and Santiago et al. (2016) presented layer jamming mechanisms that cover the surface

of snake-like and tail-like manipulators. The thin layers can keep the internal passage out of obstruction but a vacuum pump was still required as an extra power source.

Table 1. The comparison between different approaches of stiffness regulation

Stiffness regulation approach	Total length (mm)	Self-Weight (g)	Payload (N)	Deflection (mm)	Stiffness (N/mm)	Percentage change in stiffness	References
Antagonistic actuation	200	-	1.4	15	0.093	156%	(Stilli et al., 2014)
	87	-	About 1.6	2.5	0.529	219%	(Kim et al., 2014b)
Rack-locking mechanism	290	98	4.8	-	-	-	(Yagi et al., 2006)
Drive-rod-locking mechanism	200	102	2.5	59.79	0.042	165%	(Sun et al., 2020)
Central-cable-tensioning mechanism	300	34	5	-	-	-	(Degani et al., 2006)
Layer jamming	250	-	About 7	30	About 0.233	About 156%	(Moses et al., 2013)
	400	-	About 3.8	19	About 0.2	About 190%	(Kim et al., 2013)
Granular jamming	380	345	74	About 90	About 0.78	*About 925%	(Cheng et al., 2012)
	135	-	About 1.5	10	About 0.15	About 300%	(Ranzani et al., 2015)

*this paper also used additional tension cables to further strengthen the manipulator.
- Not reported.

Therefore, new methods are still required to achieve effective and reliable stiffness adjustment for a continuum robot with slender structure. In the above prototypes, rod-driven type soft continuum robots are compact, compliant and easy to control with bidirectional actuation properties. In this paper, we select this solution to develop a continuum robot with variable stiffness for potential use in soft manipulation under unstructured environments, such as rescue, space exploration, and medical devices.

Mathematical models are essential for the design and application of soft continuum robots when facing variable conditions including having their stiffness changed. Nevertheless, most previous studies focused on the kinematics and dynamics of the robot body while few models were concerned with the variable stiffness mechanisms. The kinematics models of the continuum robots are generally based on the piecewise constant-curvature assumption (Jones and Walker, 2006) and use the bending angles and the angles of bending planes to characterize the configurations (Simaan et al., 2009). These models established mappings between the actuator space, configuration space, and task space (Webster and Jones, 2010; Mahl et al., 2014). However, pure kinematic models usually ignored the effects of external loads, which limits their application.

The statics of continuum robots, taking the external forces into account, can be approximately analyzed by beam theories. Desired configurations were transformed into tendon inputs utilizing Euler-Bernoulli beam model (Camarillo et al., 2008) or Cosserat beam model (Renda et al., 2012). Beam model can also be represented by quaternions as configuration variables, which naturally incorporated inflation/extension, bending, twisting, extension, and shear deformations of extensible continuum manipulators (Tunay, 2013). These beam models usually ignored the interactions between individual robotic segments including friction and geometric constraints. Xu and Simaan (2009) combined elliptic integrals and optimization to obtain the desired

internal loads of a multi-segment continuum robot. For more general cases, the curve routing paths of the tendon were considered (Rucker and Webster, 2011), and the influence of internal friction as well as the variation in curvature were captured (Rone and Ben-Tzvi, 2014a; Rone and Ben-Tzvi, 2014b). The force-deflection relationships of multi-segment continuum robots can also be derived by lumped-mass approach (Kang et al., 2013) or compliance matrix (Qi et al., 2016) where screw theory (Dai, 2012) and Rodrigues' formula (Dai, 2015) was used. It is found that in the above static models, whether using the Newton method (Qi et al., 2016) or the virtual work principle (Rone and Ben-Tzvi, 2014a), the configuration parameters were related to Young's Modules of the robot and applied forces including actuation and external forces. However, it remains difficult to measure and control the non-uniformly distributed actuation forces along the drive cables/rods, especially when configuration and stiffness can vary in such flexible robots.

In this paper, a static model and variable stiffness mechanism are developed based on a general class of rod-driven continuum robot. The contributions of this work include: (1) Using the geometric constraint and the principle of virtual work, a static model considering the influence of actuation displacement, rod elasticity, gravity, friction, and external load is established. Compared with previous static models, it uses the actuation displacements derived from geometric constraint equations, rather than the actuation forces of the drive rods, as the inputs to predict and control body deformation under external payloads. Therefore, the problem that the non-uniformly distributed actuation forces of such continuum robots can not usually be measured is solved. Additionally, the phenomenon that the robot body can show an S-shaped curve subject to only a single-directional force is revealed. The relationship among friction, room temperature and the amplitude of current was also revealed. The signal function was used to judge if the friction forces do the virtual work. (2) A new variable stiffness mechanism with built-in SMA springs is proposed. Such mechanism can 'lock' the robot body by tuning the internal friction between the drive rods and constraint disks fixed on the central backbone.

The paper is organized as follows: Section 2 describes the statics model of a general type of rod-driven continuum robot. In section 3, the working principle of the variable stiffness mechanism and its model are revealed. Based on the above methods, a prototype of the soft continuum robot is proposed in section 4. Section 5 validates the statics model through experiments and presents the relationship between the variable friction and stiffness. Section 6 summarizes the paper and discusses future work.

2. Geometric Constraint Based Modeling and Analysis of the Generalized Rod-driven Continuum Robot

The generalized design of rod-driven continuum robots has a central backbone and M modules (sections) (Rone and Ben-Tzvi, 2014b; Simaan et al., 2009), as shown in Fig. 1. Each module is composed of three drive rods and N constraint disks, allowing for two DOF bending motion. The backbone and drive rods of the robot discussed in this paper are made of hyperelastic alloy (e.g. NiTi alloy) so that the drive rods are able to pull and push bidirectionally. The drive rods, fixed to the end disk of the

corresponding modules and moving through other constraint disks freely, can control the configuration of the continuum robot with different displacements.

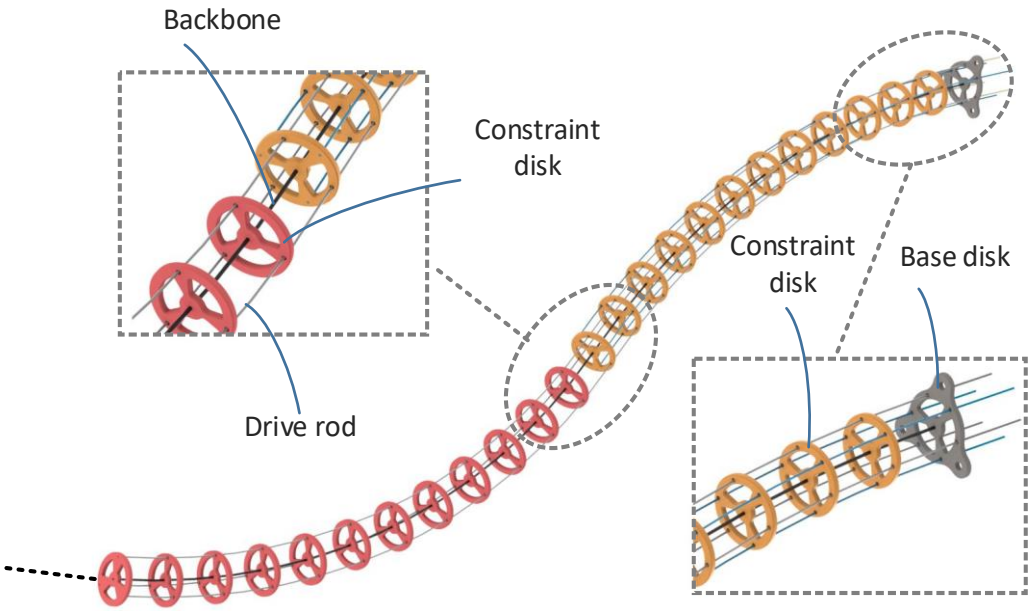

Fig.1 Generalized design of rod-driven continuum robots

2.1 Kinematic Configurations

We define the constraint disk n ($n=1,2,3\ldots,N$) of module m ($m=1,2\ldots,M$) as $disk_{m,n}$. Thus, $disk_{m,0}$ represents the base disk of module m which is also the end disk of module $m-1$, $disk_{m-1,N}$. Next, the segment between $disk_{m,n-1}$ and $disk_{m,n}$ is abbreviated as $Seg_{m,n}$. Here, we introduce a new variable u ($u=1,2,\ldots,M$) to describe the situation that the drive rod j (j =1,2,3) is fixed to the end disk of module u, which is marked as $rod_{u,j}$.

The spatial frame O_0 is fixed to the base of the continuum robot and a series of local frames $O_{m,n}$ is established at each segment as shown in Fig.2 with all of the x-axes point to the $rod_{1,1}$. Assuming each segment is a constant curvature mini-arc, the shape of $Seg_{m,n}$ can be represented by the two sets of configuration parameters $\theta_{m,n}$ and $\varphi_{m,n}$, which make up the vector $\boldsymbol{q}_{m,n}$ as

$$\boldsymbol{q}_{m,n} = \begin{bmatrix} \theta_{m,n} & \varphi_{m,n} \end{bmatrix}^{\mathrm{T}} \tag{1}$$

Integrating all the vectors, the overall robot configuration can be uniquely described by the generalized coordinate vector $\boldsymbol{q}$ as

$$\boldsymbol{q} = \begin{bmatrix} \boldsymbol{q}_{1,1}^{\mathrm{T}} & \cdots & \boldsymbol{q}_{1,N}^{\mathrm{T}} & \boldsymbol{q}_{2,1}^{\mathrm{T}} & \cdots & \boldsymbol{q}_{M,N}^{\mathrm{T}} \end{bmatrix}^{\mathrm{T}} \tag{2}$$

$\boldsymbol{T}_{m,n}$, defined as Eq.(B1) in the Appendix B, represents the transformation matrix from frame $O_{m,n-1}$ to frame $O_{m,n}$. Therefore, ${}^{1,0}\boldsymbol{T}_{m,n}$ can be derived as shown in Eq.(3) to obtain the pose $\boldsymbol{R}_{m,n}$ and position $\boldsymbol{P}_{m,n}$ of frame $O_{m,n}$.

$${}^{1,0}\boldsymbol{T}_{m,n} = \boldsymbol{T}_{1,1}\boldsymbol{T}_{1,2}\cdots\boldsymbol{T}_{1,11}\boldsymbol{T}_{2,1}\cdots\boldsymbol{T}_{m,n} = \begin{bmatrix} \boldsymbol{R}_{m,n} & \boldsymbol{P}_{m,n} \\ 0 & 1 \end{bmatrix} \tag{3}$$

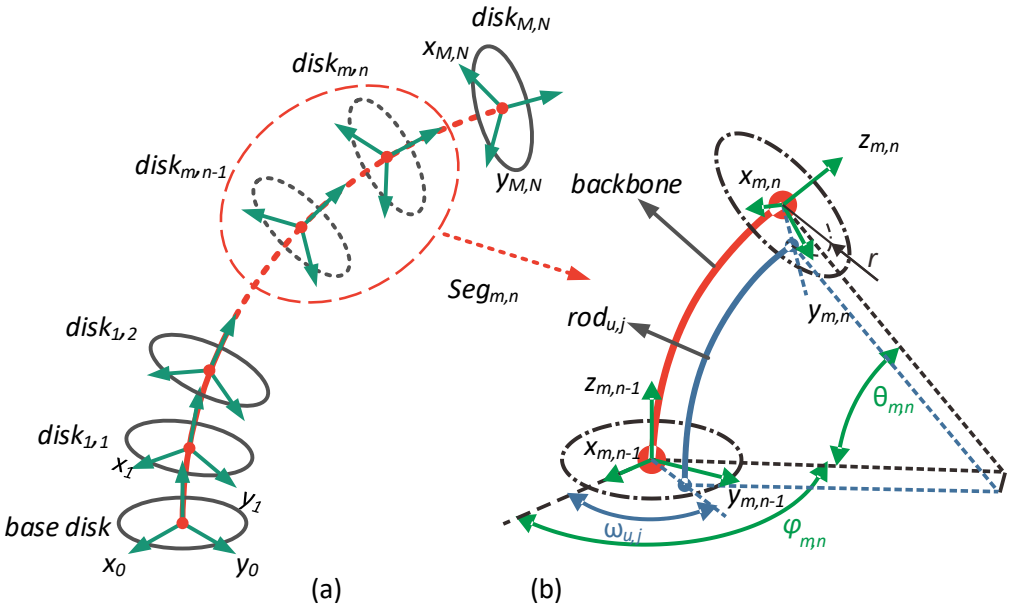

Fig.2 (a) Kinematics of the continuum robot (b) Bending configuration of $Seg_{m,n}$

2.2 Geometric Constraint

For most slender continuum robots (Xu and Simaan, 2009; Camarillo et al., 2008), their bending stiffness is lower than torsional stiffness, resulting in the assumption that the twisting deformation can be ignored in comparison to the bending deformation. Therefore, the central backbone and the drive rods are always parallel as shown in Fig. 2(b). The geometric constraint mentioned above means that the length change of $rod_{u,j}$ within the $Seg_{m,n}$ is a function of configuration parameters, which can be expressed as

$$\eta_{u,j\_m,n} = -r\theta_{m,n}\cos(\omega_{u,j} - \varphi_{m,n}) \tag{4}$$

where r and $\omega_{u,j}$ are the distribution radius and the angle relative to the x-axis of drive $rod_{u,j}$, respectively. The three drive rods of each module are evenly distributed on a circle with radius r, which means $\omega_{u,j+1} - \omega_{u,j} = 2\pi/3$.

In addition, the relative sliding displacement between $rod_{u,j}$ and $disk_{m,n}$ is denoted as $D_{u,j\_m,n}$ and obtained by

$$\begin{aligned} D_{u,j\_m,n} &= \sum_{\bar{n}=n+1}^{N} \eta_{u,j\_m,\bar{n}} \qquad (u = m) \\ D_{u,j\_m,n} &= \sum_{\bar{m}=m+1}^{u} \sum_{\bar{n}=1}^{N} \eta_{u,j\_\bar{m},\bar{n}} + \sum_{\bar{n}=n+1}^{N} \eta_{u,j\_m,\bar{n}} \qquad (u > m) \end{aligned} \tag{5}$$

where $D_{u,j\_m,N} = 0$ $(m=u)$ since the drive rods are fixed at the end disks of each module. When $disk_{1,0}$ is considered, the relative sliding displacement $D_{u,j\_1,0}$ is simplified as $D_{u,j}$, representing the actuation displacement of the $rod_{u,j}$, i.e. the total length displacement of the drive rod. Thus, the geometric constraint is also reflected by Eq.(5) showing that the sum of length change in individual segments equals the actuation displacement. If there are three drive rods for each of the two degrees of freedom modules, the redundancy of the third drive rod $D_{u,3}$ can be expressed as

$$D_{u,3} = a_{u,3}D_{u,1} + b_{u,3}D_{u,2} \tag{6}$$

where $a_{u,3}$ and $b_{u,3}$ are the coefficients, which can be obtained by Eq.(B2) and (B3) in the Appendix B. The above-described geometric constraint not only reflects the

relationship between each actuation displacement and the resulting configuration of the continuum robot but also reduces the dependence of the static model on the actuation forces as shown in the following sections.

2.3 Statics Analysis Based on the Principle of Virtual Work

A typical configuration of the continuum robot under static equilibrium is shown in Fig.3, and the virtual work of the system δW under the virtual displacement $\delta \boldsymbol{q}$ is established as

$$\delta W = \delta W_{\text{el}} + \delta W_{\text{ac}} + \delta W_{\text{gr}} + \delta W_{\text{lo}} = 0 \tag{7}$$

where δW_{el}, δW_{ac}, δW_{gr}, and δW_{lo} represent the virtual works of elastic force, actuation force, gravity and external load, respectively.

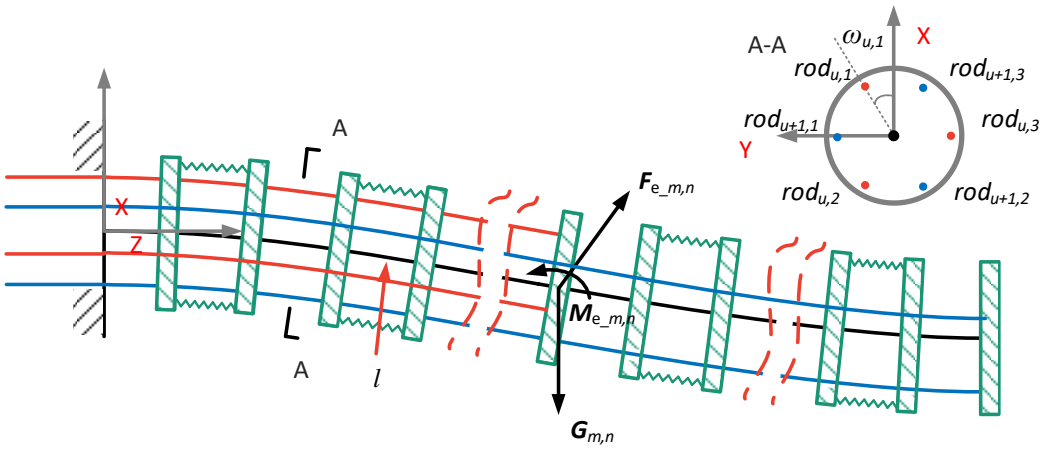

Fig.3 Static equilibrium of the continuum robot

2.3.1 The Elastic Force: The central backbone and the drive rods made of the hyperelastic alloy are considered as Euler-Bernoulli beams with linear and isotropic relations between stain and stress (Nemat-Nasser and Guo, 2006). The virtual work of internal elastic forces, δW_{el}, can be derived by summing the virtual work of the backbone and drive rods of each module as

$$\delta W_{\text{el}} = -\sum_{m=1}^{M}\sum_{n=1}^{N} M_{m,n} l \delta\kappa_{m,n} - \sum_{m=1}^{M}\sum_{n=1}^{N}\sum_{u=\text{m}}^{M}\sum_{j=1}^{3} M_{u,j\_m,n}\left(l + \eta_{u,j\_m,n}\right)\delta\kappa_{u,j\_m,n} \tag{8}$$

where $M_{m,n}$ and $M_{u,j\_m,n,}$ indicate bending moments of backbone and the $rod_{u,j}$ within $Seg_{m,n}$, and $\kappa_{m,n}$ and $\kappa_{u,j\_m,n}$ are the corresponding curvatures. All of these quantities are functions of $\theta_{m,n}$ as Eq.(B4) to Eq.(B7) shown in the Appendix B. l is the backbone length of every segment.

2.3.2 The Actuation Force: As mentioned in Section 2.2, there are just two independent drive rods for each module. Therefore, the actuation force of the robot can be equivalent to the tension or pressure of two drive rods in module u marked as $\tau_{u,1}$ and $\tau_{u,2}$. The corresponding actuation displacements $D_{u,1}$ and $D_{u,2}$ are obtained from Eq.(5). The virtual work of the actuation force, δW_{ac}, accumulates the virtual work of equivalent actuation forces in two drive rods as

$$\delta W_{\text{ac}} = \sum_{u=1}^{M}\left(\tau_{u,1}\delta D_{u,1} + \tau_{u,2}\delta D_{u,2}\right) \tag{9}$$

Note that, in this paper, although the actuation force of each drive rod is considered in the model, its value does not need to be known because of the introduction of geometric constraints.

2.3.3 The Gravity Effect: The gravity of the constraint disk is G, and the density of the hyperelastic alloy used as the backbone and the drive rod is ρ with their center of gravity $\boldsymbol{C}_{m,n}$ approximately located in the middle of $Seg_{m,n}$, which can be expressed as

$$\boldsymbol{C}_{m,n} = \boldsymbol{P}_{m,n} - \boldsymbol{P}_{m,n-1} \tag{10}$$

where $\boldsymbol{P}_{m,n}$, obtained from Eq.(3), represents position of $disk_{m,k}$. d_{ba} and d_{ro} represent the diameter of backbone and the drive rods, respectively. Then, the virtual work of gravity, δW_{gr}, including the virtual work of gravity of constraint disks, backbone, and rods can be derived as

$$\delta W_{\mathrm{gr}} = \sum_{m=1}^{M}\sum_{n=1}^{N}\left(G\delta \boldsymbol{P}_{m,n} + \left(\frac{\pi l \rho \left(d_{ba}^2 + 3d_{ro}^2 \right)}{4} + \frac{\pi \rho d_{ro}^2}{4} \sum_{u=m}^{M}\sum_{j=1}^{3} \eta_{u,j\_m,n} \right) \delta \boldsymbol{C}_{m,n} \right) \tag{11}$$

2.3.4 The External Load: The virtual work of external load, δW_{lo}, accumulates the virtual work of external loads and moments as

$$\delta W_{\mathrm{lo}} = \sum_{m=1}^{M}\sum_{n=1}^{N}\left(\boldsymbol{F}_{\mathrm{e}\_m,n}\delta \boldsymbol{P}_{m,n} + \boldsymbol{M}_{\mathrm{e}\_m,k}\delta \boldsymbol{A}_{m,n} \right) \tag{12}$$

where $\boldsymbol{F}_{\mathrm{e}\_m,n}$ and $\boldsymbol{M}_{\mathrm{e}\_m,n}$ as shown in Fig. 3, represent the external load and the external couple acting on $disk_{m,n}$, respectively. The term $\delta \boldsymbol{A}_{m,n}$ represents the virtual angular displacement and the $\boldsymbol{A}_{m,n}$ can be obtained from Eq.(B8) in the Appendix B.

2.4 The Equilibrium Equation of the Generalized Rod-Driven Continuum Robot

The virtual displacements in Eq.(8), (9), (10), (11) and (12) are functions of the generalized coordinates $\boldsymbol{q}$. Eq.(7) can be transformed into the product of generalized force $\boldsymbol{Q}$ and generalized coordinate virtual displacement $\delta \boldsymbol{q}$ as

$$\delta W = \sum_{t=1}^{Len(\boldsymbol{q})} (Q_{\mathrm{el},t} + Q_{\mathrm{ac},t} + Q_{\mathrm{gr},t} + Q_{\mathrm{lo},t})\delta \boldsymbol{q}(t) = 0 \tag{13}$$

where $Len(\boldsymbol{q})$ is the length of $\boldsymbol{q}$. $\boldsymbol{Q}_{\mathrm{el},t}$, $\boldsymbol{Q}_{\mathrm{ac},t}$, $\boldsymbol{Q}_{\mathrm{gr},t}$, $\boldsymbol{Q}_{\mathrm{lo},t}$ are generalized elastic forces, actuation force, gravity, external load, respectively as Eq. (B9) shows in the Appendix B. However, except $\boldsymbol{q}$, there are still $2 \times M$ unknowns, the actuation forces $\tau_{u,1}$, $\tau_{u,2}$ (u=1,2,..M) in Eq.(13). Unlike the actuation forces given by the sensors in the conventional static model, this paper takes the actuation displacement of drive rod that derived from the geometric constraint as the input. Considering the redundancy, only two inputs are required for each module, so an additional $2 \times M$ equations can be derived from Eq.(4) and Eq.(5), as shown in Eq.(14). By combining Eq. (14) with Eq. (13), the configuration parameters $\theta_{m,n}$ and $\varphi_{m,n}$ in each local frame can be solved for.

$$D_{u,j} = -\sum_{m=1}^{u}\sum_{n=1}^{N} r\theta_{m,n} \cos\left(\omega_{u,j} - \varphi_{m,n} \right), \ (j = 1,2), (u = 1,2,...M) \tag{14}$$

3. Modeling and Analysis with SMA Initiated Variable Stiffness

3.1 Variable Stiffness Mechanism

Based on the generalized rod-driven continuum robot design, we propose a stiffness regulation mechanism that can change the friction between the drive rods and constraint disks. Unlike the antagonistic actuators or central-cable-tensioning methods, which apply a longitudinal force at the tip to stiffen the entire manipulator, possibly leading to uneven internal forces at individual segments/joints, our design uses distributed mechanisms along the continuum manipulator to achieve local stiffness regulation for individual segments.

As shown in Fig. 4(a), there are three groups of levers assembled on a pair of adjacent constraint disks. SMA springs are utilized to drive the levers due to their high power-weight ratio, flexibility and compactness that are suitable for implementation in such a slender, narrow space. Each group of levers is pulled by one SMA spring through a thread tension mechanism shown in Fig.4 (b). In the unlocked mode, when the SMA spring and thread are loose, there is no force applied to the corresponding lever on the upper and lower constraint disks and the drive rods can move freely. In the locked mode, the SMA spring is heated by electrical current, I, and therefore pull two threads at both ends with a tension of F_t. The thread goes through the constraint disk and lever through a curved hole. Once it is tensioned, it will apply a force F_1 to one end of the corresponding lever at point B. So the lever will rotate about the pivot, C, and apply a force F_2 to the other end, A, and therefore clamp the drive rods to the corresponding constraint disk shown in Fig.4 (c). In this way, we can use three SMA springs to lock the rod's movement on two adjacent constraint disks. By increasing the current to the SMA springs, the contact force to the drive rods and the friction between the rods and constraint disks will be increased until they are locked together, which means the overall stiffness of the continuum robot increases.

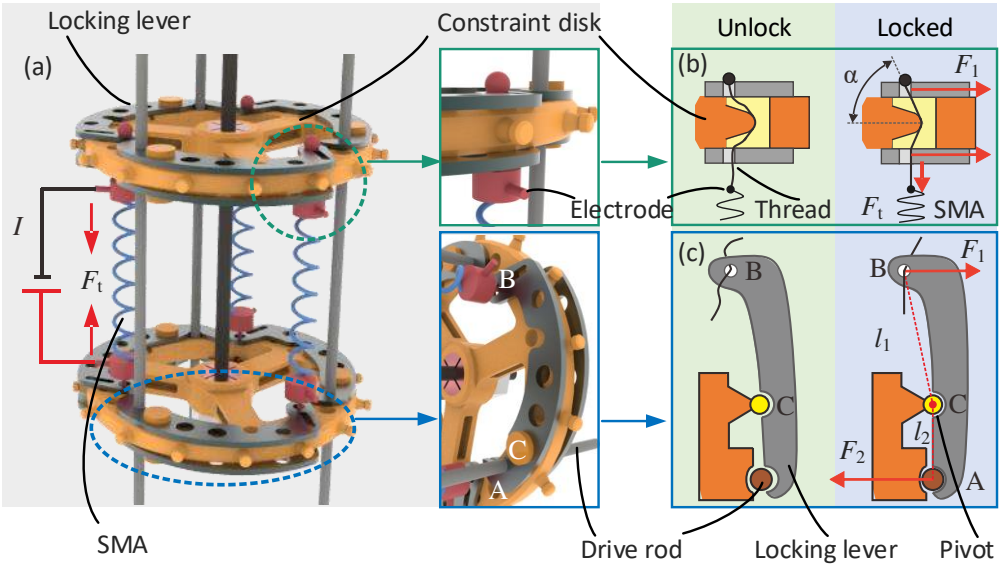

Fig.4 Leverage mechanism for stiffness adjustment

3.2 The Tensions of SMA: When the stiffness of the proposed continuum robot changes, new variables such as the tension of the SMA and the resulting frictional force

will be introduced. The SMA spring between $disk_{m,n-1}$ and $disk_{m,n}$ is abbreviated as $SMA_{j\_m,n}$ as shown in Fig.5. Here, n can only take even numbers since every two adjacent constraint disks share one SMA. Then, the position of upper fixed point $H_{j\_m,n}$ of $SMA_{j\_m,n}$ in $disk_{m,n}$ can be deduced by the following equation

$$\boldsymbol{H}_{j\_m,n} = \boldsymbol{R}_{m,n}\begin{bmatrix} r\cos\Omega_{u,j} & r\sin\Omega_{u,j} & 0 \end{bmatrix}^{\mathrm{T}} + \boldsymbol{P}_{m,n} \tag{15}$$

where r is the distribution radius of SMA spring, and $\Omega_{u,j}$ is the distribution angle of $SMA_{j\_m,n}$ relative to x-axis and $\Omega_{u,j} - \omega_{u,j} \approx 2\pi/3$. $l_{j\_m,n}$ is the length of $SMA_{j\_m,n}$, which can be obtained from Eq.(16).

$$l_{j\_m,n} = \left\| \boldsymbol{H}_{j\_m,n} - \boldsymbol{H}_{j\_m,n-1} \right\| \tag{16}$$

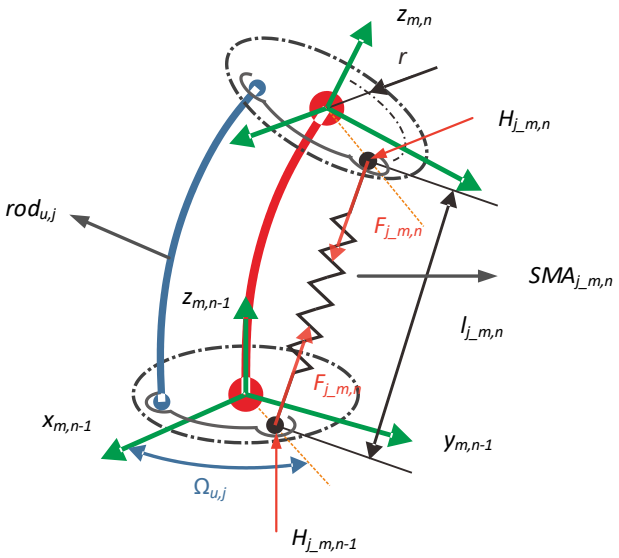

Fig.5 SMA springs of stiffness regulating mechanism

Additionally, the tension $F_{j\_m,n}$ of SMA spring is also related to the temperature T as

$$F_{j\_m,n} = \frac{G_T d_s}{8k^3 N_s}\left(l_{j\_m,n} - l_{\mathrm{SMA}}\right) \tag{17}$$

$$\boldsymbol{F}_{j\_m,n} = -\boldsymbol{F}_{j\_m,n-1} = \frac{\boldsymbol{H}_{j\_m,n} - \boldsymbol{H}_{j\_m,n-1}}{l_{j\_m,n}} F_{j\_m,n} \tag{18}$$

where G_T is the shear modulus that changes with temperature (Liang and Rogers, 1990; An et al., 2012) and it remains constant when $T > 80$°C (Ma et al., 2010; Salerno et al., 2016). d_s is the diameter of the SMA spring, k is the spring index of SMA, N_s is the number of turns, $l_{j\_m,n}$ is the length of the SMA spring from Eq.(16) and l_{SMA} is the original length of the SMA spring. When the SMA spring resistance R_s is fixed, the relationship between temperature T_w of SMA and the electric current I is deduced at room temperature T_0 as Eq. (19), where h_s is the coefficient of heat transfer.

$$T_w = \frac{I^2 R_s}{h_s N_s k d_s^2 \pi^2} + T_0 \tag{19}$$

The virtual work of the tension of SMA spring, δW_{sma}, can be derived from the sum of the products of the virtual displacement $\delta \boldsymbol{H}_{j\_m,n}$ and the tension $\boldsymbol{F}_{j\_m,n}$ of the SMA spring as

$$\delta W_{\text{sma}} = \sum_{m=1}^{M} \sum_{n=1}^{N} \sum_{j=1}^{3} \left(\boldsymbol{F}_{j\_m,n} \delta \boldsymbol{H}_{j\_m,n} \right) \tag{20}$$

3.3 The Friction: The tension of the SMA makes the friction between $rod_{u,j}$ and $disk_{m,n}$ increase rapidly, where $u=m$ is considered because the $rod_{u,j}$ is not locked with constraint disk in other modules. Therefore, the virtual work of internal friction, δW_{fr}, accumulates all the virtual work of sliding friction between the drive rods and the constraint disks as

$$\delta W_{\text{fr}} = \sum_{m=1}^{M} \sum_{n=1}^{N} \sum_{j=1}^{3} \left(-\text{sgn}\left(D_{u,j\_m,n} \right) f_{j\_m,n} \delta D_{u,j\_m,n} \right), \quad (u = m) \tag{21}$$

It is difficult to directly judge whether all friction forces are sliding friction to do virtual work, so sgn($D_{u,j\_m,n}$) is used to estimate the utility and direction of the friction. If $D_{u,j\_m,n}$=0, it shows that the drive rod and the constraint disk never slide at the contact point. Therefore, there is no virtual work of static friction and the virtual work is mapped into 0 by sign function sgn. If $D_{u,j\_m,n} \neq 0$, there is still a trend of sliding with sliding friction rather than an ideal constraint so that the virtual work should be considered, and the sign function extracts the sliding direction.

If there is sliding friction, we can use $f_{j\_m,n-1} = f_{j\_m,n}$ (n=even number), which is the function of the tension of SMA $F_{j\_m,n}$ (presented as F_t in Fig.4) and can be obtained as

$$f_{j\_m,n-1} = f_{j\_m,n} = 2\mu \cos\alpha \frac{l_1}{l_2} F_{j\_m,n} \tag{22}$$

where l_1 and l_2 are the lever arms, μ is the friction coefficient, and α is the winding angle of the wire.

3.4 The Equilibrium Equation Considering the SMA-Based Stiffness Regulation

Like the equilibrium equation proposed in Section 2.4, here we introduce the virtual displacements in Eq. (20), (21), which are also functions of the generalized coordinates $\boldsymbol{q}$. Eq. (13) can be rewritten as

$$\delta W = \sum_{t=1}^{Len(\boldsymbol{q})} (Q_{\text{el},t} + Q_{\text{ac},t} + Q_{\text{gr},t} + Q_{\text{lo},t} + Q_{\text{sma},t} + Q_{\text{fr},t}) \delta \boldsymbol{q}(t) = 0 \tag{23}$$

where $\boldsymbol{Q}_{\text{sma},t}$, $\boldsymbol{Q}_{\text{fr},t}$ are generalized tensions of SMA springs, and sliding friction, respectively as Eq. (B10) shows in the Appendix B.

4. The Variable-Stiffness Based Soft Continuum Robot

4.1 The New Continuum Manipulator

Based on the design mentioned above, a prototype is designed, which consists of a variable stiffness continuum manipulator, an end effector, an actuation box, and an

electric cabinet as shown in Fig.6. The design aims to manipulate targets and tune the stiffness of the main body in unstructured environments. There are two modules included and each module is composed of a central backbone, three drive rods evenly distributed 120 degrees apart, and eleven constraint disks. The NiTi alloy is assigned as the backbone and the drive rods. The manipulator has a total length of 880mm and an outer diameter of 38mm, which is covered with a nylon mesh. Note that the nylon mesh skin covering the constraint disks will limit the twisting deformation of the arm. The end effector is mounted on the top of the manipulator and is capable of being replaced for different tasks. In this paper, a three-fingered gripper driven by a linear motor is used. A camera (ZBS-001, EBOSI corp., China) providing vision is embedded in the center of the gripper. The electromagnetic sensor (3D Guidance trakSTAR, Northern Digital Inc., Canada) can detect and return its position in the magnetic field, which was established by the transmitter. Since the point on the backbone cannot be directly measured, both sides of the cross section of the constraint disk were measured, and the midpoint of them can be calculated and recognized as the centroid of the constraint disk on the backbone.

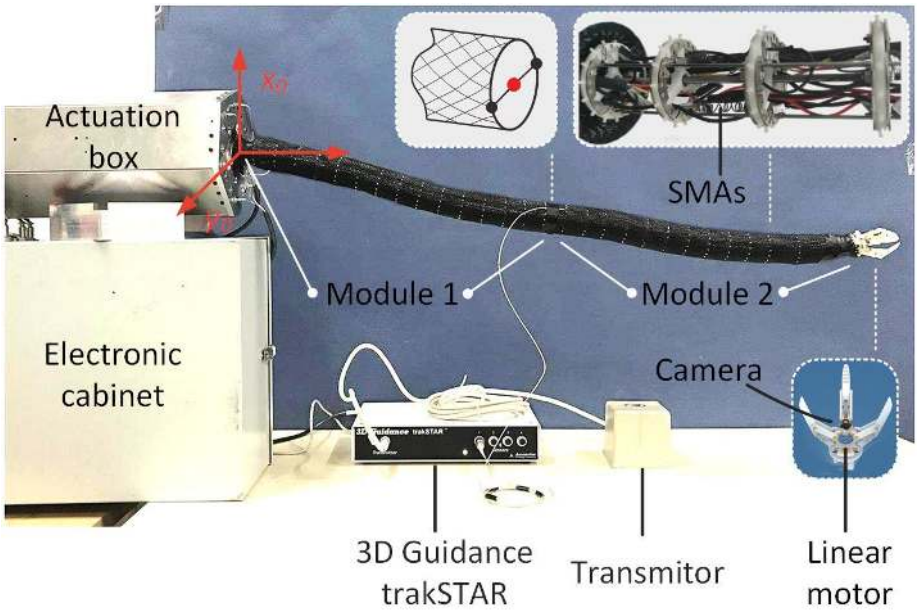

Fig.6 Prototype and measurement platform

4.2 Rod-driven Actuation

As shown in Fig. 7, the entire actuation box can be divided into two parts. The right half contains six screw slider mechanisms transmitting the rotational motion of the motors to the linear motion of the drive rods. In order to detect the tension and compression on the rods, force sensors (MBZY-1, ZN Corp., China) are installed on each slider at a symmetrical position to the drive rod through an equal-arm lever mechanism. This design makes external load detection feasible. The left half is used to arrange the corresponding motors (RE25, Maxon motor AG, Switzerland) and their drivers.

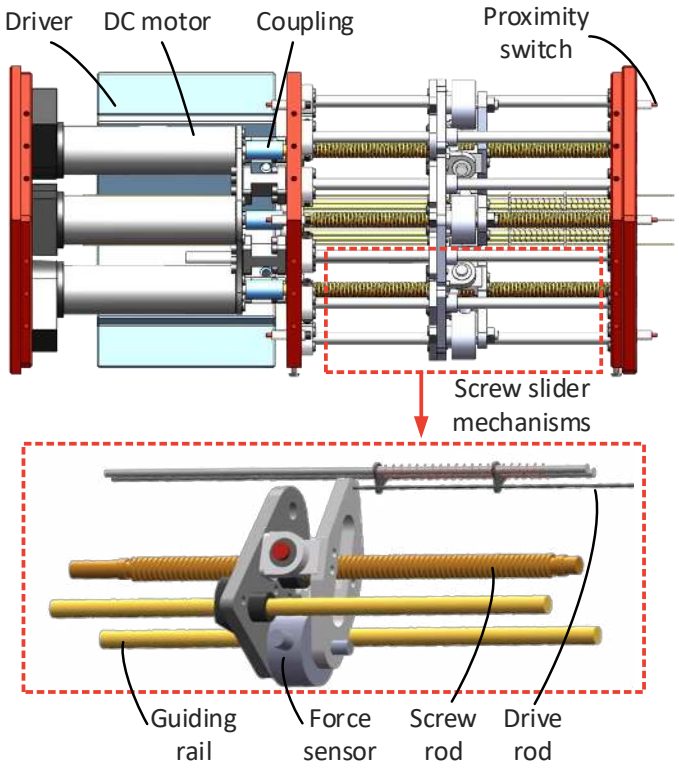

Fig.7 Structure and composition of the actuation box

The control system consists of a PC and various control objects linked by a CAN bus as shown in Fig.8. The configuration and stiffness control routines are coded in the VC++ language and run on the PC. The controlled objects mentioned include six DC brush motors, data acquisition cards (ICAN-4017, GHD Corp., China), and a linear motor (LC1574AQ, China) for the gripper. The data acquisition card can collect the analog signals of force sensors and output the signal for SMA current regulation.

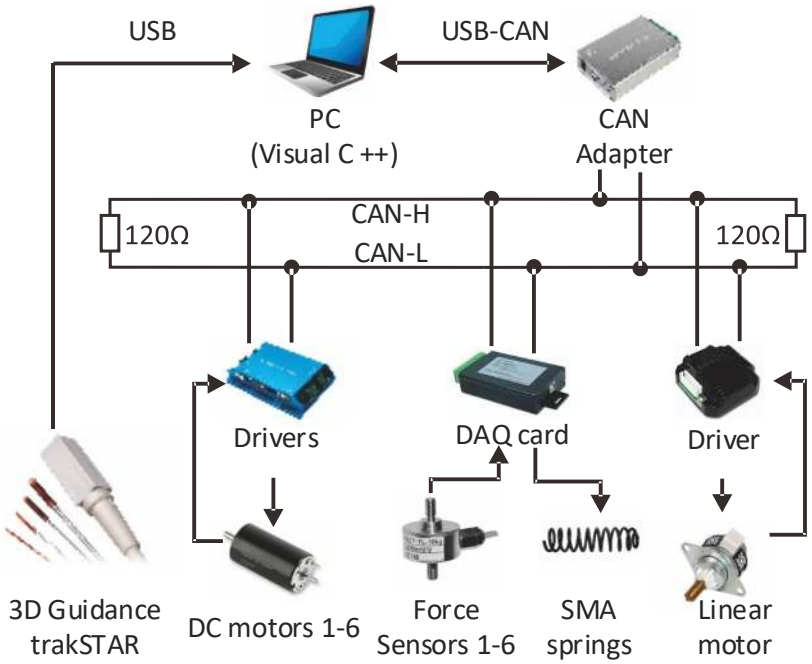

Fig.8 Block diagram of the control system

4.3 Specifications of the Continuum Robot

The geometric and material parameters of the presented continuum manipulator are detailed in Table 2.

Table 2 Material and geometric parameters of the prototype

	Property	Value		Property	Value
E	Young's Modulus of NiTi alloy	160 Gpa	h_s	A coefficient of heat transfer	6.3W/(m^2·℃)
ρ	Density of NiTi alloy	6.5g/cm^{-3}	R_s	Resistance of SMA	1 Ω
I_{ba}	Backbone radial moment of inertia	0.78mm^{-4}	α	Turning angle of Wire	π/3
I_{ro}	Drive rod radial moment of inertia	0.25mm^{-4}	k	Spring index of SMA	9
G	Gravity of constraint disk	5×10^{-3} kg	N_s	SMA spring number of turns	30
μ	Coefficient of friction	1	D_s	SMA spring diameter	4.5 mm
G_T	The shear modulus of SMA spring	*35 G*Pa ⩾ 80℃	d_{ba}	The diameter of backbone	2 mm
r	Distribution radius of SMA and rods	15 mm	d_{ro}	The diameter of drive rods	1.5 mm
$\omega_{1,1}$	Angle between $rod_{1,1}$ and x-axis	*0*	l	Length of Segment	40 mm
$\omega_{2,1}$	Angle between $rod_{2,1}$ and x-axis	π/3	T_0	Room temperature	20 ℃

5. Effect of Variation of Actuation Displacement, External Load and Stiffness

In this section, a series of simulations with different actuation inputs and external loads were implemented and compared against experimental results. In addition, the influence of the internal friction on the stiffness was demonstrated through simulation and experiment. To simplify the results, the deformation of the manipulator is represented by the curve of its backbone.

5.1 Effect of Change of Actuation Displacement With Zero External Load: In this case, four sets of actuation displacements are given without external loads as the inputs, which is $\boldsymbol{D}_{u,j}$ =[4, -2, -2, 2, -4, 2] (the resulting configuration is referred to as configuration 1.1 and marked as Conf. 1.1), $\boldsymbol{D}_{u,j}$ =[-4, 2, 2, -2, 4, -2] (Conf. 1.2), $\boldsymbol{D}_{u,j}$ =[2, 2, -4, 4, -2, -2] (Conf. 1.3) and $\boldsymbol{D}_{u,j}$ =[2, -4, 2, -2, -2, 4] (Conf. 1.4). As a reference, Conf. 0 is also presented, which is the initial state of the manipulator $\boldsymbol{D}_{u,j}$ =[0, 0, 0,0, 0, 0] but only under gravity as shown in Fig. 9. The red line, blue dashed line and gray circle present the deformation of module 1 and module 2 in simulations and the results of experiments, respectively. If only kinematics are considered, Conf. 1.1 and Conf. 1.2 are symmetric about (0, 0, 880), yet due to gravity, the endpoint positions are all shifted toward the negative direction of the x-axis, whose positions obtained by simulations and experiments are listed as Table 3. The results show that in this case, the ratio of the positioning error at the manipulator tip to its length, defined as error ratio, is less than 1.83%.

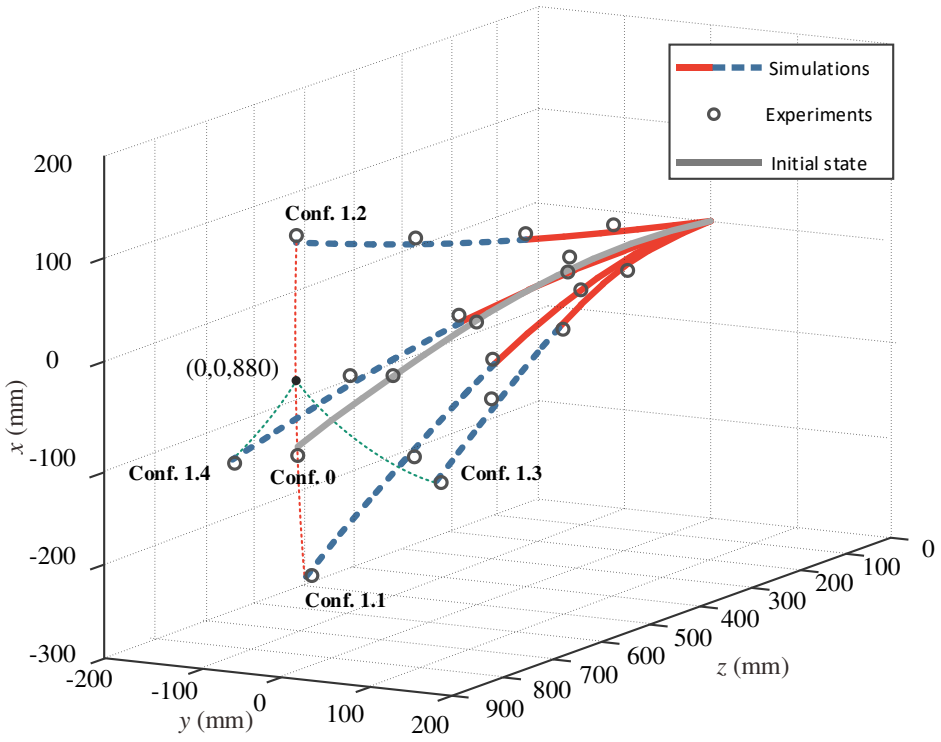

Fig.9 Deformations under different actuation displacement

Table 3 Results of endpoint under different actuation displacement

Configurations	Conf 0	Conf 1.1	Conf 1.2	Conf 1.3	Conf 1.4
Experiments	(-53.6, 0.0, 876.3)	(-220.6, 2.6, 856.2)	(126.4, 3.2, 873.4)	(-102.3, 110.2, 879.5)	(-105.3, -116.5, 880.4)
Simulations	(-58.9, 1.5, 891.5)	(-215.6, 0.0, 861.4)	(119.6, 0.0, 870.2)	(-110.4, 115.2, 875.4)	(-112.3, -113.2, 876.8)
Deviation	16.1	7.6	8.16	10.4	8.5
Error ratio	1.83%	0.86%	0.93%	1.18%	0.97%

5.2 Effect of Change of External Load with the Stand-Still Actuation Displacement: In this case, the actuation displacement of all the drive rods is given to be zero ($D_{u,j}$=0), to obtain the deformation of the manipulator under identical external loads acting on different points in the x-z plane. Firstly, $\boldsymbol{F}$=-3N is applied to the midpoint (Conf. 2.1) and the endpoint (Conf. 2.2) of the manipulator respectively, then $\boldsymbol{F}$=3N is applied to the midpoint (Conf. 2.3) and the endpoint (Conf. 2.4) of the manipulator respectively, as shown in Fig.10. It can be seen that the closer the load force F is to the end, the larger the deflection of the manipulator generated. In addition, the deformations of the Conf. 2.1 and Conf. 2.3 as well as the Conf. 2.2 and Conf. 2.4 are almost symmetric but with a slight difference due to gravity.

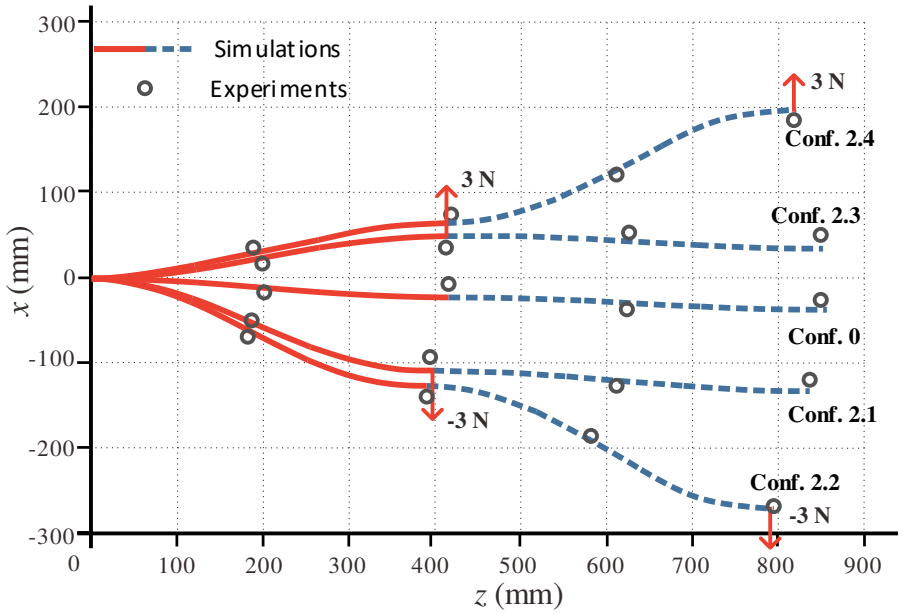

Fig.10 Deformations under loads acting on different points

Next, we keep the actuation displacement at zero and change the value of the external loads where all of them are applied on the endpoint. The $\boldsymbol{F}$= -0.5 (Conf. 2.5), $\boldsymbol{F}$= -1 (Conf. 2.6), $\boldsymbol{F}$= 0.5 (Conf. 2.7) and $\boldsymbol{F}$= 1 (Conf. 2.8) are exerted as shown in Fig.11. With the increase of the value of $\boldsymbol{F}$, the displacement of the endpoint on the x-axis becomes larger, and the manipulator shows a double 'S-shaped' curve.

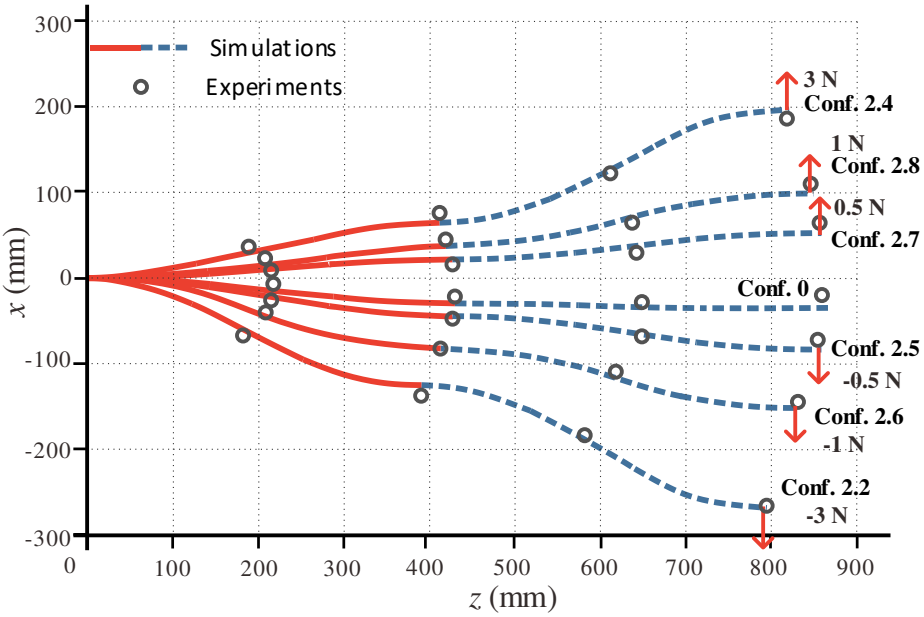

Fig.11 Deformations under the different value of loads

Figure 11 not only reveals the effects of different loads on the deformation but also shows the phenomenon that each module of the manipulator presents an S-shaped curve rather than a C-shaped curve usually observed in a cantilever beam. As the external load increases, the S-shape becomes more obvious. This is because we limit all the actuation displacements $D_{u,j}$=0. According to the geometric constraint given by Eq.(5), an S-shaped manipulator allows for different local length change of a drive rod in

individual segments, but the total length change of the drive rod keeps constant. If the manipulator bends in a C-shape, the local length of a drive rod in all segments will simultaneously become larger or smaller depending on which side (dorsal or ventral) the drive rod locates on, which is not consistent with the geometric constraints.

5.3 Effect of Different Actuation Displacement with External Loads: In this case, the performance of the manipulator under the same external load, $\boldsymbol{F}$ = -1N at the end disk, but with different actuation displacement are shown. To better compare the results under different conditions, all the actuation displacement make the robot only bend in the *x*-*z* plane. The $\boldsymbol{D}_{u,j}$ =[0, 0, 0, 5, -10, 5] (Conf. 3.1), $\boldsymbol{D}_{u,j}$ =[5, -2.5, -2.5, 5, -10, 5] (Conf. 3.2), $\boldsymbol{D}_{u,j}$ =[0, 0, 0, -5, 10, -5] (Conf. 3.3), $\boldsymbol{D}_{u,j}$ =[-5, 2.5, 2.5, -7.5, 15, -7.5] (Conf. 3.4) and $\boldsymbol{D}_{u,j}$ =[-10, 5, 5, -10, 20, -10] (Conf. 3.5) are presented in Fig.12 respectively. For comparison, Conf. 2.6 is also introduced with $\boldsymbol{D}_{u,j}$ =[0, 0, 0, 0, 0, 0]. In addition, the actuation displacement of the first module of Conf. 3.1 and Conf. 3.3 keep also zero, so their first module shows an S-shape curve. Fig.12 shows that if the bending direction of two modules is the same, the larger the actuation displacement input was given, the larger deflection of the manipulator exhibited.

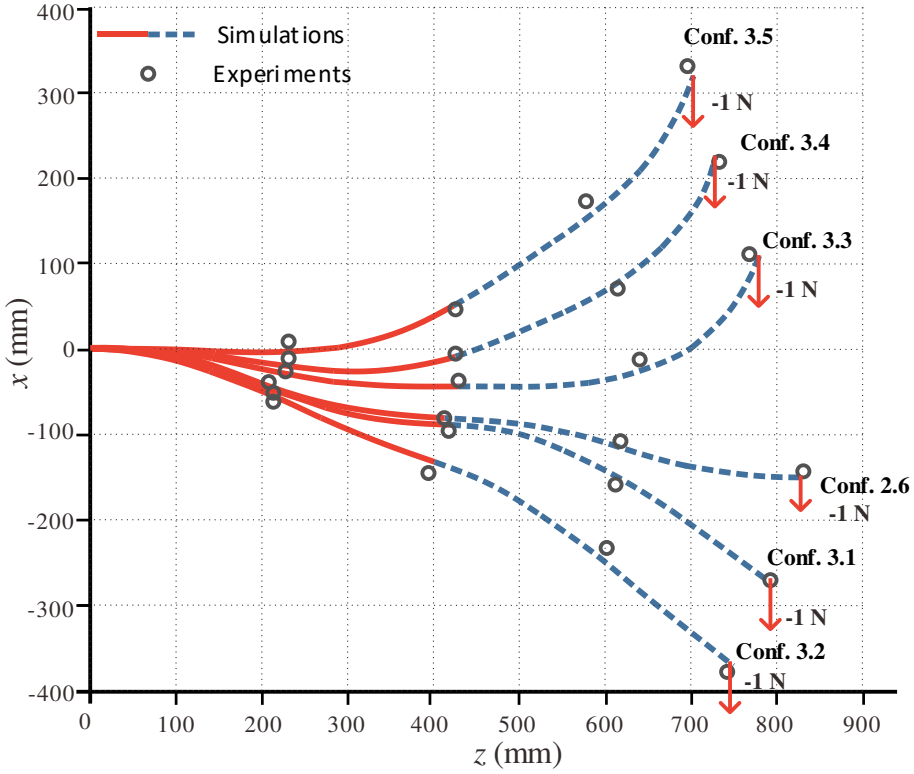

Fig.12 Deformations under same direction bends

Moreover, $\boldsymbol{D}_{u,j}$ =[5, -2.5, -2.5, -2.5, 5, -2.5] (Conf. 3.6), $\boldsymbol{D}_{u,j}$ =[10, -5, -5, -2.5, 5, -2.5] (Conf. 3.7), $\boldsymbol{D}_{u,j}$ =[10, -5, -5, 0, 0, 0] (Conf. 3.8), $\boldsymbol{D}_{u,j}$ =[-5, 2.5, 2.5, 2.5, -5, 2.5] (Conf. 3.9), $\boldsymbol{D}_{u,j}$ =[-10, 5, 5, 2.5, -5, 2.5] (Conf. 3.10) and $\boldsymbol{D}_{u,j}$ =[-20, 10, 10, 2.5, -5, 2.5] (Conf. 3.11) are shown in Fig.13, respectively, which makes the first module and the second module bend in opposite directions. Similarly, the simulation results obtained by the proposed model are well matched with the experimental results. In particular, at the

Conf. 3.8, the actuation displacements of module 2 $\boldsymbol{D}_{2,j}$ = [0, 0, 0], but it still presents an upward curve due to the downward curve of module 1.

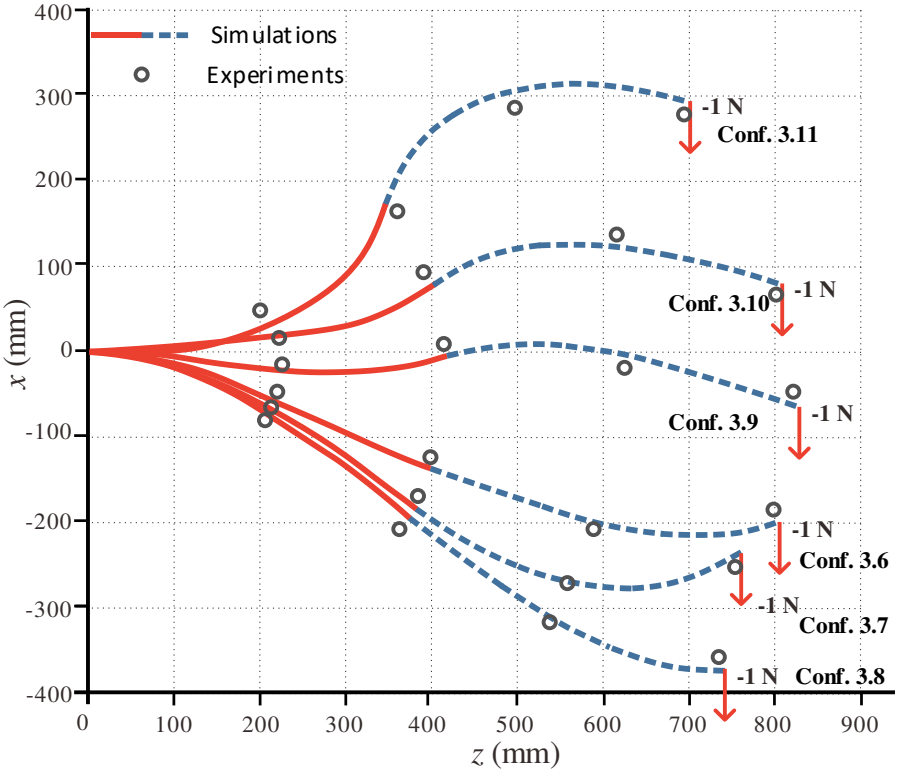

Fig.13 Deformations under different direction bends

It can be noted from the above three cases that the deformations of the simulations are close to the experiments, but there still are some errors, which may be caused by some assumptions mentioned in Section 2. The maximum deviation occurred in Conf. 3.5 with a position error at the endpoint of 19.6mm and the error ratio is 2.23%.

5.4 Effect of Variable Stiffness Demonstration and Validation

As mentioned in Section 3, the stiffness of the manipulator can be improved by increasing the internal friction, whose relationship can also be solved by using the proposed statics model with actuation displacement inputs. According to Eq.(22), the maximum sliding friction depends on the electric current I of the SMA springs. Therefore, in this case, the deformation of the manipulator obtained by experiments and simulations under the same end load 100g but different electric currents are shown in Fig.14 and Fig.15, respectively. Conf. 0 (0N, 0A) is the initial state without payload. Then, if F=1N is exerted at the endpoint, its configuration changes to Conf. 2.6 (-1N, 0A) with a displacement in the x-axis of 158.2mm in the experiment at the endpoint. However, if the currents are applied before the payload, the deformation will change to Conf. 4.1(-1N, 0.5A), Conf. 4.2(-1N, 1A) and Conf. 4.3(-1N, 2A), with the corresponding displacement in the x-axis of 132.5mm, 91.6mm and 68.7mm, respectively. In addition, we found that the SMA springs have little effect on the configuration of the continuum manipulator because the tension of SMA springs are local and applied to all drive rods.

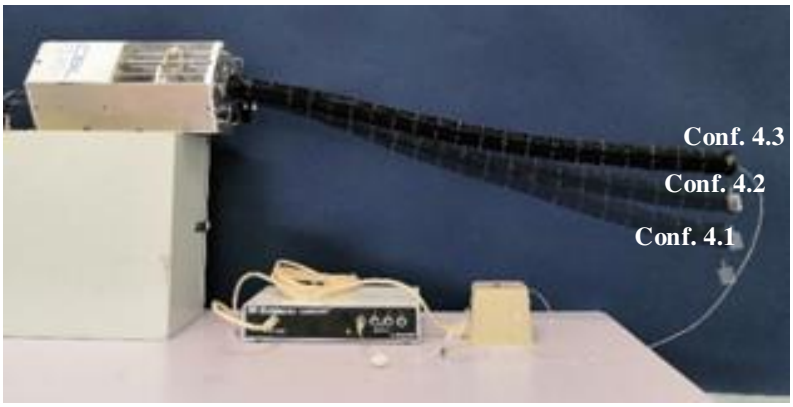

Fig.14 Physical demonstration of the stiffness adjustment under 100g end load

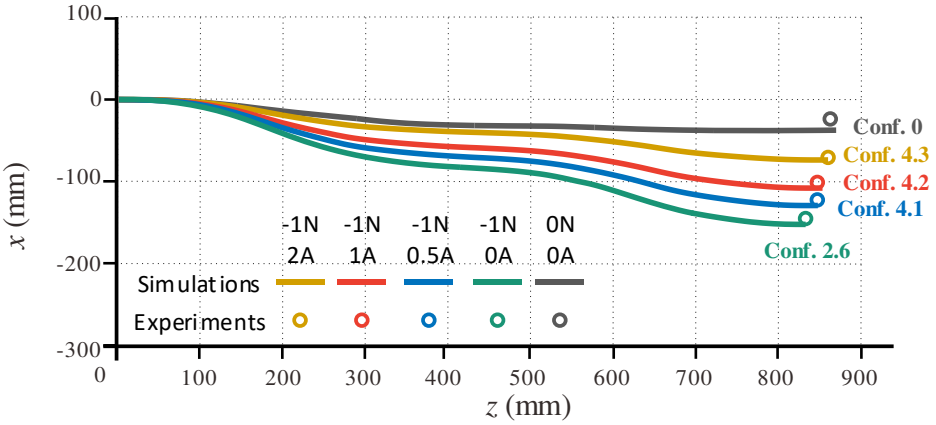

Fig.15 Simulation and experiments under 100g end load with variable stiffness

Furthermore, keeping the initial condition as Conf. 0, we change the magnitude of the end load and plot the relationship of payload and displacement under different currents, as is shown in Fig. 16. It can be seen that the modulation of current does promote the ability of the manipulator to maintain the desired configuration. The quotient between the $\Delta \boldsymbol{F}$ and the corresponding $\Delta \boldsymbol{x}$, as shown in the Eq. (24), is used to characterize the stiffness of the manipulator.

$$\boldsymbol{K} = \frac{\Delta \boldsymbol{F}}{\Delta x} \tag{24}$$

When external loads are lower than 1.5 N, a nonlinear relationship can be observed and the stiffness will decrease slightly with the increase of external loads. This is because, first, the constitutive model of the NiTi alloy itself conforms to this trend. Another factor is that the internal static friction provided by the stiffening mechanism is not enough to resist the deformation of the manipulator. However, when the external loads are greater than 1.5N, the stiffness of the manipulator increases again and approximates to a constant indicating that the load has less influence on the stiffness under this situation. This is because, since the actuation displacement of all the drive rods are limited to zero, this geometric constraint converts into a motion constraint, which exerts a non-negligible influence on the mechanical properties of the manipulator. Under this condition, when the external load is 3N, the currents of 2A, 1A and 0.5A can increase the stiffness of the manipulator by 287%, 192% and 121%, respectively.

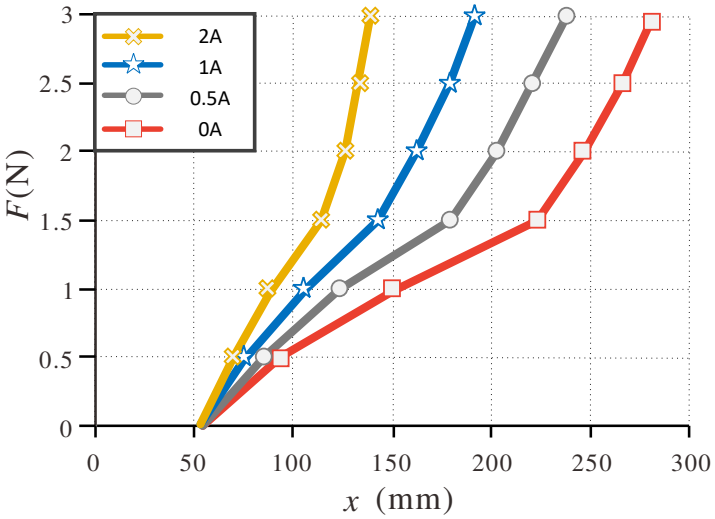

Fig.16 Relationship between the end load and displacement

5.5 Discussion on the variable stiffness performance

The main structure of our continuum manipulator is composed of the NiTi alloy with its intrinsic compliance and light weight. The total length and the weight are 880mm and 137g, respectively. Before its stiffness is changed, the deflection of the manipulator is 54mm when under gravity (Conf. 0). Then it increases to 287mm when subjected to an extra payload of 3N (Conf. 2.2), and the stiffness is 0.0129N/mm according to Eq. (24). By heating the SMA springs with a current of 2A, the deflection under the same payload becomes 135mm, and the stiffness increases 287% to 0.0370N/mm. In this situation, the external load is 2.2 times the weight of the manipulator and the deflection is 15.3% of the manipulator length. 3N payload is considered as the upper limit of this prototype as shown in Fig. 16. If the external load is increased further, the large deflection will make it difficult to control the manipulator.

Compared with previous variable stiffness continuum robots summarized in Table 1, the percentage change in stiffness, 287%, of our manipulator is at a relatively high level. However, the absolute stiffness of our manipulator may initially appear to not be so impressive. This can however be explained by using beam theory (Boresi et al., 1985). If a continuum manipulator is approximately considered as a cantilever, the stiffness at the tip and load capacity are inversely proportional to the cubic of its total length. Considering our manipulator has a much greater length than others, we believe the results are good.

In addition, we observe that the SMA material has some limitations, such as the hysteresis, low control accuracy, and long cooling time. However, compared with position control requirements (usually at millimeter level for positioning and second level for response time (Webster and Jones, 2010)) for this type of manipulator, the stiffness control does not require very high precision and speed. It is usually allowable for the continuum manipulator to spend some time stiffening its body after reaching the desired position. In this paper, the SMA springs can reach the phase-transition temperature within 1–2 seconds by applying a current of 2A and the stiffness of the manipulator will soon have a significant increase in 5–6 seconds. On the other hand, at

room temperature around 20 degrees Celsius, the SMA spring will take about 22–29 seconds to cool down and unload the internal stress, which is also acceptable.

6 Conclusions

This paper introduced an SMA-spring-based stiffness regulating mechanism for a new rod-driven continuum robot. The friction along the drive-rods are then adjusted by electric current applied to the SMA springs, that the desired robot configuration can be maintained.

In the analysis, a new static model based on both virtual work and geometric constraint was established and took for the first time both adjustable friction force and tension of the SMA into account. Therefore, the performance before and after stiffness regulation can be obtained. The paper in particular demonstrated that the geometric constraints contained two parts. One is the length change of drive rods as function of two sets of configuration parameters within individual segments and two is the sum of the length changes in each segment is equal to the actuation displacement. The geometric constraints in such rod-driven type continuum robots help solve the statics without a measurement of actuation force. Further, it was found that the robot under an external load will exhibit an S-shaped curve to meet the above geometric constraints. The experimental validations showed that the maximum error ratio of the continuum robot is 2.23%.

The proposed stiffness regulation mechanism and the virtual-work based static model present a new way for design and analysis of continuum robots for use in detection and maintenance tasks in unconstructed environments, e.g. turbine engines, satellites, nuclear plant and so on. Future work will implement micro grooves to the portion of the drive rod that is in contact with the lever mechanism, so that high friction or even complete locking will be achieved between the lever and drive rods. The effects of the twisting motion will be assessed and incorporated in the analytical model. These will further improve the variable stiffness performance of our prototype and the accuracy of the model.

Acknowledgment

The financial support from the National Key R&D Program of China (Grant No. 2018YFB1304600), the Natural Science Foundation of China (Grant No. 51875393, No. 51535008 and No. 51721003), the International Collaboration Program (Grant No. B16034), and the State Key Laboratory of Robotics Foundation-China (Grant No. 2019-O04) are greatly acknowledged.

Appendix A: Index to Multimedia Extensions

Table of Multimedia Extensions

Extension	Media type	Description
1	video	Video shows that the continuum robot grasps a ping-pong ball avoiding the obstacle
2	video	Video shows the actuation, transmission and control systems of the continuum robot
3	video	Video shows how the variable stiffness mechanism works
4	video	Video shows the double "S-shaped" curve of the robot

Appendix B: Equation Derivation of the Variables in the Text

The transformation matrices from frame $O_{m,n-1}$ to frame $O_{m,n}$ and l is the backbone length of $Seg_{m,n}$.

$$\boldsymbol{T}_{m,n} = Rot_z\left(\varphi_{m,n}\right) Tr_x\left(\frac{l}{\theta_{m,n}}\right) Rot_y\left(\theta_{m,n}\right) Tr_x\left(\frac{-l}{\theta_{m,n}}\right) Rot_z\left(-\varphi_{m,n}\right) \tag{B1}$$

The coefficients of redundant actuation displacement

$$a_{u,3} = \frac{\tan\omega_{u,2}\cos\omega_{u,3} - \sin\omega_{u,3}}{\tan\omega_{u,2}\cos\omega_{u,1} - \sin\omega_{u,1}} \tag{B2}$$

$$b_{u,3} = \frac{\tan\omega_{u,1}\cos\omega_{u,3} - \sin\omega_{u,3}}{\tan\omega_{u,1}\cos\omega_{u,2} - \sin\omega_{u,2}} \tag{B3}$$

The bending moments of backbone and $rod_{u,j}$ within $Seg_{m,n}$

$$M_{m,n} = EI_{\mathrm{ba}}\kappa_{m,n} \tag{B4}$$

$$M_{u,j\_m,n} = EI_{\mathrm{ro}}\kappa_{u,j\_m,n} \tag{B5}$$

The curvatures of backbone and $rod_{u,j}$ within $Seg_{m,n}$

$$\kappa_{m,n} = \frac{\theta_{m,n}}{l} \tag{B6}$$

$$\kappa_{u,j\_m,n} = \frac{\theta_{m,n}}{l\left(1-\cos\left(\omega_{u,j}-\varphi_{m,n}\right)\right)} \tag{B7}$$

The Euler angles of frame $O_{m,n}$

$$\boldsymbol{A}_{m,n} = \left[\arctan\left(\frac{\boldsymbol{R}^{21}_{m,n}}{\boldsymbol{R}^{11}_{m,n}}\right) \quad \arctan\left(\frac{\boldsymbol{R}^{32}_{m,n}}{\boldsymbol{R}^{33}_{m,n}}\right) \quad \arctan\left(\frac{\boldsymbol{R}^{31}_{m,n}}{\sqrt{\left(\boldsymbol{R}^{32}_{m,n}\right)^2 + \left(\boldsymbol{R}^{33}_{m,n}\right)^2}}\right)\right]^{\mathrm{T}} \tag{B8}$$

The generalized force $\boldsymbol{Q}$

$$\begin{cases} Q_{\mathrm{el},t} = -\sum_{m=1}^{M}\sum_{n=1}^{N}\dfrac{\partial\left(M_{m,n}\kappa_{m,n}\right)}{\partial \boldsymbol{q}(t)}l - \sum_{m=1}^{M}\sum_{n=1}^{N}\sum_{u=\mathrm{m}}^{M}\sum_{j=1}^{3}\dfrac{\partial\left(M_{u,j\_m,n}\left(l+\eta_{u,j\_m,n}\right)\kappa_{u,j\_m,n}\right)}{\partial \boldsymbol{q}(t)} \\ Q_{\mathrm{ac},t} = \sum_{u=1}^{M}\left(\tau_{u,1}\dfrac{\partial D_{u,1}}{\partial \boldsymbol{q}(t)} + \tau_{u,2}\dfrac{\partial D_{u,2}}{\partial \boldsymbol{q}(t)}\right) \\ Q_{\mathrm{gr},t} = \sum_{m=1}^{M}\sum_{n=1}^{N}\left(G\dfrac{\partial \boldsymbol{P}_{m,n}}{\partial \boldsymbol{q}(t)} + \dfrac{\pi l\rho\left(d_{ba}^2+3d_{ro}^2\right)}{4}\dfrac{\partial \boldsymbol{C}_{m,n}}{\partial \boldsymbol{q}(t)} + \dfrac{\pi\rho d_{ro}^2}{4}\dfrac{\partial\left(\boldsymbol{C}_{m,n}\sum_{u=m}^{M}\sum_{j=1}^{3}\eta_{u,j\_m,n}\right)}{\partial \boldsymbol{q}(t)}\right) \\ Q_{\mathrm{lo},t} = \sum_{m=1}^{M}\sum_{n=1}^{N}\left(\boldsymbol{F}_{e\_m,n}\dfrac{\partial \boldsymbol{P}_{m,n}}{\boldsymbol{q}(t)} + \boldsymbol{M}_{e\_m,n}\dfrac{\partial \boldsymbol{A}_{m,n}}{\boldsymbol{q}(t)}\right) \end{cases} \tag{B9}$$

$$\begin{cases} Q_{\mathrm{sma},t} = \sum_{m=1}^{M}\sum_{n=1}^{N}\sum_{j=1}^{3}\dfrac{\partial\left(\boldsymbol{F}_{j\_m,n}\boldsymbol{H}_{j\_m,n}\right)}{\boldsymbol{q}(t)} \\ Q_{\mathrm{fr},t} = \sum_{m=1}^{M}\sum_{n=1}^{N}\sum_{j=1}^{3}\left(-\mathrm{sgn}\left(D_{m,j\_m,n}\right)\dfrac{\partial\left(f_{j\_m,n}D_{m,j\_m,n}\right)}{\boldsymbol{q}(t)}\right) \end{cases} \tag{B10}$$

Nomenclature

$disk_{m,n}$	The constraint disk n ($n=1,2,\ldots,N$) of module m ($m=1,2,\ldots,M$)
$Seg_{m,n}$	The segment between $disk_{m,n-1}$ and $disk_{m,n}$
$rod_{u,j}$	The drive rod j (j =1,2,3) is fixed to the end disk of module u
O_0	The spatial frame
$O_{m,n}$	The local frames
$\boldsymbol{q}_{m,n}$	The configuration parameter of $Seg_{m,n}$
${}^{1,0}\boldsymbol{T}_{m,n}$	The transformation matrix from frame $O_{1,0}$ to frame $O_{m,n}$
$\boldsymbol{T}_{m,n}$	The transformation matrix from frame $O_{m,n-1}$ to frame $O_{m,n}$
$\boldsymbol{R}_{m,n}$	The pose of frame $O_{m,n}$
$\boldsymbol{P}_{m,n}$	The position of frame $O_{m,n}$
$\boldsymbol{A}_{m,n}$	The angular displacement of frame $O_{m,n}$
$\eta_{u,j\_m,n}$	The length change of $rod_{u,j}$ within the $Seg_{m,n}$
r	The distribution radius of drive rod and the SMA spring
$\omega_{u,j}$	The angle relative to the x-axis of drive $rod_{u,j}$
$D_{u,j}$	The actuation displacement of the $rod_{u,j}$
δW	The virtual work of the system

$\delta \boldsymbol{q}$	The virtual displacement
$M_{m,n}$	The bending moment of backbone within $Seg_{m,n}$
$M_{u,j\_m,n}$	The bending moment of the $rod_{u,j}$ within $Seg_{m,n}$
$\kappa_{m,n}$	The curvature of backbone within $Seg_{m,n}$
$\kappa_{u,j\_m,n}$	The curvature of backbone within $Seg_{m,n}$
I_{ba}	The backbone radial moment of inertia
I_{ro}	The drive rod radial moment of inertia
d_{ba}, d_{ro}	The diameter of backbone and drive rod
E	Young's Modulus of NiTi alloy
l	The backbone length of every segment
$\tau_{u,j}$	The equivalent forces of drive $rod_{u,j}$
G	The gravity of constraint disk
$\boldsymbol{C}_{m,n}$	The center of gravity of backbone and drive rod within $Seg_{m,n}$
ρ	The density of the NiTi alloy
$\boldsymbol{F}_{\mathrm{e}\_m,n}$	The external load acting on $disk_{m,n}$
$\boldsymbol{M}_{\mathrm{e}\_m,n}$	The external couple acting on $disk_{m,n}$
$SMA_{j\_m,n}$	The jth SMA spring between $disk_{m,\mathrm{n-1}}$ and $disk_{m,n}$
$H_{j\_m,n}$	The position of fixed point of $SMA_{j\_m,n}$ in $disk_{m,n}$
$\Omega_{u,j}$	The distribution angle of $SMA_{j\_m,n}$ relative to x-axis
$l_{j\_m,n}$	The length of $SMA_{j\_m,n}$
$F_{j\_m,n}$	The tension of $SMA_{j\_m,n}$
T_w	The temperature of SMA spring
G_T	The shear modulus of SMA spring
d_s	The diameter of SMA spring
k	The spring index of SMA spring
N_s	The number of turns of SMA spring
R_s	the SMA spring resistance
I	The electric current in SMA spring
h_s	The coefficient of heat transfer
$f_{j\_m,n}$	The sliding friction between the drive rods and the constraint disks

l_1 , l_2	The length of lever arms of stiffening mechanisms
μ	The friction coefficient of stiffening mechanisms
α	The winding angle of the wire of stiffening mechanisms
$\boldsymbol{Q}$	The generalized force of robot
$\boldsymbol{q}$	The generalized coordinates of robot

References

An S-M, Ryu J, Cho M and Cho K-J. (2012) Engineering design framework for a shape memory alloy coil spring actuator using a static two-state model. *Smart Materials and Structures* 21: 055009.

Bajo A and Simaan N. (2016) Hybrid motion/force control of multi-backbone continuum robots. *The International Journal of Robotics Research* 35: 422-434.

Boresi AP, Schmidt RJ and Sidebottom OM. (1985) *Advanced mechanics of materials*: Wiley New York et al.

Camarillo DB, Milne CF, Carlson CR, Zinn MR and Salisbury JK. (2008) Mechanics Modeling of Tendon-Driven Continuum Manipulators. *Ieee Transactions on Robotics* 24: 1262-1273.

Catalano MG, Grioli G, Farnioli E, Serio A, Piazza C and Bicchi A. (2014) Adaptive synergies for the design and control of the Pisa/IIT SoftHand. *International Journal of Robotics Research* 33: 768-782.

Chen Y, Chang JH, Greenlee AS, Cheung KC, Slocum AH and Gupta R. (2010) Multi-turn, Tension-stiffening Catheter Navigation System. *2010 IEEE International Conference on Robotics and Automation (ICRA).* 5570-5575.

Cheng NG, Lobovsky MB, Keating SJ, Setapen AM, Gero KI, Hosoi AE and Iagnemma KD. (2012) Design and Analysis of a Robust, Low-cost, Highly Articulated Manipulator Enabled by Jamming of Granular Media. *2012 IEEE International Conference on Robotics and Automation (ICRA).* 4328-4333.

Cianchetti M, Tommaso R, Gerboni G, Nanayakkara T, Althoefer K, Dasgupta P and Menciassi A. (2014) Soft Robotics Technologies to Address Shortcomings in Today's Minimally Invasive Surgery: The STIFF-FLOP Approach. *Soft Robotics* 1: 122-131.

Dai JS. (2012) Finite Displacement Screw Operators With Embedded Chasles' Motion. *Journal of Mechanisms and Robotics* 4: 041002-041002-041009.

Dai JS. (2015) Euler–Rodrigues formula variations, quaternion conjugation and intrinsic connections. *Mechanism and Machine Theory* 92: 144-152.

Dai JS and Ding X. (2005) Compliance Analysis of a Three-Legged Rigidly-Connected Platform Device. *Journal of Mechanical Design* 128: 755-764.

Degani A, Choset H, Wolf A and Zenati M. (2006) Highly Articulated Robotic Probe for Minimally Invasive Surgery. *2006 IEEE International Conference on Robotics and Automation (ICRA).* 4167- 4172.

Deimel R and Brock O. (2016) A novel type of compliant and underactuated robotic hand for dexterous grasping. *International Journal of Robotics Research* 35: 161-185.

Dong X, Axinte D, Palmer D, Cobos S, Raffles M, Rabani A and Kell J. (2017) Development of a slender continuum robotic system for on-wing inspection/repair of gas turbine engines. *Robotics and Computer-Integrated Manufacturing* 44: 218-229.

Dupont PE, Lock J, Itkowitz B and Butler E. (2010) Design and Control of Concentric-Tube Robots. *Ieee Transactions on Robotics* 26: 209-225.

G.Robinson and Davies JBC. (1999) Continuum Robots—A State of the Art. *1999 IEEE International Conference on Robotics and Automation (ICRA).* 2849-2854.

Hawkes EW, Blumenschein LH, Greer JD and Okamura AM. (2017) A soft robot that navigates its environment through growth. *Science Robotics* 2: eaan3028.

Jones BA and Walker ID. (2006) Kinematics for multisection continuum robots. *Ieee Transactions on Robotics* 22: 43-55.

Kang R, Branson DT, Zheng T, Guglielmino E and Caldwell DG. (2013) Design, Modeling and Control of a Pneumatically Actuated Manipulator Inspired By Biological Continuum Structures. *Bioinspiration & Biomimetics* 8: 036008.

Kato T, Okumura I, Song SE, Golby AJ and Hata N. (2015) Tendon-Driven Continuum Robot for Endoscopic Surgery: Preclinical Development and Validation of a Tension Propagation Model. *Ieee-Asme Transactions on Mechatronics* 20: 2252-2263.

Kim RH, Kang CH, Bae JH and Kang BS. (2014a) Development of a Continuum Robot using Pneumatic Artificial Muscles. *2014 IEEE International Conference on Control, Automation and Systems*: 1401-1403.

Kim Y, Cheng S, Kim S and Iagnemma K. (2014b) A Stiffness-Adjustable Hyperredundant Manipulator Using a Variable Neutral-Line Mechanism for Minimally Invasive Surgery. *Ieee Transactions on Robotics* 30: 382-395.

Kim YJ, Cheng SB, Kim S and Iagnemma K. (2013) A Novel Layer Jamming Mechanism With Tunable Stiffness Capability for Minimally Invasive Surgery. *Ieee Transactions on Robotics* 29: 1031-1042.

Liang C and Rogers CA. (1990) One-Dimensional Thermomechanical Constitutive Relations for Shape Memory Materials. *Journal of Intelligent Material Systems and Structures* 1: 207-234.

Ma J, Karaman I and Noebe RD. (2010) High temperature shape memory alloys. *International Materials Reviews* 55: 257-315.

Mahl T, Hildebrandt A and Sawodny O. (2014) A variable curvature continuum kinematics for kinematic control of the bionic handling assistant. *Ieee Transactions on Robotics* 30: 935-949.

Mahvash M and Dupont PE. (2011) Stiffness Control of Surgical Continuum Manipulators. *Ieee Transactions on Robotics* 27: 334-345.

McMahan W, Jones BA and Walker ID. (2005) Design and Implementation of a Multi-Section Continuum Robot: Air-Octor. *2005 IEEE/RSJ International Conference on Intelligent Robots and Systems (IROS).* 2578-2585.

Moses MS, Kutzer MDM, Hans M and Armand M. (2013) A continuum manipulator made of interlocking fibers. *2013 IEEE International Conference on Robotics and Automation.* 4008-4015.

Nemat-Nasser S and Guo W. (2006) Superelastic and Cyclic Response of NiTi SMA at Various Strain Rates and Temperatures. *Mechanics of materials* 38: 463-474.

Qi P, Qiu C, Liu H, Dai JS, Seneviratne LD and Althoefer K. (2016) A Novel Continuum Manipulator Design Using Serially Connected Double-Layer Planar Springs. *IEEE/ASME Transactions on Mechatronics* 21: 1281-1292.

Ranzani T, Gerboni G, Cianchetti M and Menciassi A. (2015) A bioinspired soft manipulator for minimally invasive surgery. *Bioinspiration & Biomimetics* 10: 035008.

Renda F, Cianchetti M, Giorelli M, Arienti A and Laschi C. (2012) A 3D steady-state model of a tendon-driven continuum soft manipulator inspired by the octopus arm. *Bioinspiration & Biomimetics* 7: 025006.

Rone WS and Ben-Tzvi P. (2014a) Continuum Robot Dynamics Utilizing the Principle of Virtual Power. *Ieee Transactions on Robotics* 30: 275-287.

Rone WS and Ben-Tzvi P. (2014b) Mechanics Modeling of Multisegment Rod-Driven Continuum Robots. *Journal of Mechanisms and Robotics* 6.

Rucker DC, Jones BA and Webster RJ. (2010) A Geometrically Exact Model for Externally Loaded Concentric-Tube Continuum Robots. *Ieee Transactions on Robotics* 26: 769-780.

Rucker DC and Webster RJ. (2011) Statics and Dynamics of Continuum Robots With General Tendon Routing and External Loading. *Ieee Transactions on Robotics* 27: 1033-1044.

Salerno M, Zhang K, Menciassi A and Dai JS. (2016) A Novel 4-DOF Origami Grasper With an SMA-Actuation System for Minimally Invasive Surgery. *Ieee Transactions on Robotics* 32: 484-498.

Santiago JLC, Godage IS, Gonthina P and Walker ID. (2016) Soft Robots and Kangaroo Tails: Modulating Compliance in Continuum Structures Through Mechanical Layer Jamming. *Soft Robotics* 3: 54-63.

Simaan N, Xu K, Wei W, Kapoor A, Kazanzides P, Taylor R and Flint P. (2009) Design and Integration of a Telerobotic System for Minimally Invasive Surgery of the Throat. *International Journal of Robotics Research* 28: 1134-1153.

Stilli A, Wurdemann HA and Althoefer K. (2014) Shrinkable, stiffness-controllable soft manipulator based on a bio-inspired antagonistic actuation principle. *2014 IEEE/RSJ International Conference on Intelligent Robots and Systems (IROS).* 2476-2481.

Sun C, Chen L, Liu J, Dai JS and Kang R. (2020) A hybrid continuum robot based on pneumatic muscles with embedded elastic rods. *Proceedings of the Institution of Mechanical Engineers, Part C: Journal of Mechanical Engineering Science* 234: 318-328.

Tunay I. (2013) Spatial Continuum Models of Rods Undergoing Large Deformation and Inflation. *Ieee Transactions on Robotics* 29: 297-307.

Walker ID, Dawson DM, Flash T, Grasso FW, Hanlon RT, Hochner B, Kier WM, Pagano CC, Rahn CD and Zhang QM. (2005) Continuum robot arms inspired by cephalopods. *Unmanned Ground Vehicle Technology VII* 5804: 303-314.

Webster RJ and Jones BA. (2010) Design and Kinematic Modeling of Constant Curvature Continuum Robots: A Review. *International Journal of Robotics Research* 29: 1661-1683.

Webster RJ, Romano JM and Cowan NJ. (2009) Mechanics of Precurved-Tube Continuum Robots. *Ieee Transactions on Robotics* 25: 67-78.

Xu K and Simaan N. (2009) Analytic Formulation for Kinematics, Statics, and Shape Restoration of Multibackbone Continuum Robots Via Elliptic Integrals. *Journal of Mechanisms and Robotics* 2: 011006.

Yagi A, Matsumiya K, Masamune K, Liao H and Dohi T. (2006) Rigid-Flexible Outer Sheath Model Using Slider Linkage Locking Mechanism and Air Pressure for Endoscopic Surgery. *2006 International Conference on Medical Image Computing and Computer-Assisted Intervention.* Berlin, Heidelberg: Springer Berlin Heidelberg, 503-510.

Zhang K, Qiu C and Dai JS. (2016) An Extensible Continuum Robot With Integrated Origami Parallel Modules. *Journal of Mechanisms and Robotics* 8: 031010-031010-031019.